Nanoscale visualization of metallic electrodeposition in a well-controlled chemical environment

ABSTRACT

Liquid phase transmission electron microscopy (TEM) provides a useful means to study a wide range of dynamics in solution with near-atomic spatial resolution and sub-microsecond temporal resolution. However, it is still a challenge to control the chemical environment (such as the flow of liquid, flow rate, and the liquid composition) in a liquid cell, and evaluate its effect on the various dynamic phenomena. In this work, we have systematically demonstrated the flow performance of an in-situ liquid TEM system, which is based on "on-chip flow" driving by external pressure pumps. We studied the effects of different chemical environment in the liquid cell as well as the electrochemical potential on the deposition and dissolution behavior of Cu crystals. The results show that uniform Cu deposition can be obtained at a higher liquid flow rate (1.38 μL min^{-1}), while at a lower liquid flow rate (0.1 μL min^{-1}), the growth of Cu dendrites was observed. Dendrite formation could be further promoted by in-situ addition of foreign ions, such as phosphates. The generality of this technique was confirmed by studying Zn electrodeposition. Our direct observations not only provide new insights into understanding the nucleation and growth, but also give guidelines for the design and synthesis of desired nanostructures for specific applications. Finally, the capability of controlling the chemical environment adds another dimension to the existing liquid phase TEM technique, extending the possibilities to study a wide range of dynamic phenomena in liquid media.

Keywords: Liquid phase transmission electron microscopy; Chemical environment; Electrodeposition; Morphology

1. Introduction

Metallic nanostructures have remarkable electronic, optical and catalytic properties, and thus a broad range of applications in biomedicine, sensors, energy storage and conversion devices.[1, 2] To tailor these physical and chemical properties and optimise the performance, different structural parameters and chemical composition of the metallic nanostructures are tuned by controlling the nucleation and growth during the synthesis process or by post-synthesis treatment.[3, 4] Among the various structural parameters, surface morphology plays a crucial role in determining performance. Taking Cu nanostructure, an important electrocatalyst for the electrochemical reduction of CO_2, as a typical example, the exposed facets or the surface atom arrangements of a single crystal catalyst affect not only the activity but also the product selectivity.[5, 6] Recent experimental and theoretical studies show that electrocatalysts with dendritic morphology possess improved electrocatalytic CO_2 reduction activity compared to ones with other morphologies.[7-10] This improvement is mainly related to the increased electric field and mass concentration at the dendritic tips induced by the high-curvature effect.[11] Although dendrites are useful in the fields of electrocatalysis, they are not desirable in other applications, such as lithium metal batteries and zinc ion batteries.[12, 13] In such case the formation of lithium or zinc dendrites during continuous cycling leads to irreversible capacity loss. It is therefore of crucial importance to understand and control the morphology of metallic nanostructures, depending on the application.

Electrochemical deposition of metallic nanostructures has several benefits compared to other preparation methods,[14, 15] including the processing at room temperature and easy scalability of the products. Most importantly, the microstructure of the deposition can be well controlled by simply changing the electrochemical parameters and the electrolyte composition. In previous studies, by manipulating deposition current density, we demonstrated that the growth direction (or exposed

crystalline facets) of metal and semiconductor nanostructures can be selected,[16, 17] which can be well understood by a modified critical dimension model.[16, 17] Moreover, inorganic ion or organic ligand addition affects the nucleation rate and surface energy of the stable nuclei by selective adsorption, and thus determines the final morphology of the deposition.[18-20] For example, the addition of Cl^- ions in $CuSO_4$ electrolyte induces the formation of Cu_2O cubes,[21] while adding $H_2PO_4^-$ ions facilitates the growth of Cu dendrites.[15] Although electrocrystallization theory can be employed to understand these results, it is still a challenge to control the morphology of the products without direct observation of the deposition process, especially at the nanoscale.

Recently, in-situ transmission electron microscopy (TEM), combined with liquid cells, has been successfully employed to study a wide range of liquid processes with near-atomic spatial resolution and sub-microsecond scale temporal resolution.[22] The liquid cells contain thin and electron transparent membranes from silicon nitride [23] or atomically thin 2D materials.[24] The liquid can be pre-sealed during the cell preparation or flowed through an external liquid tubing.[25-27] By tuning the experimental parameters such as electron flux, external biasing or/and heating, and/or mixing additional liquid, the liquid phase dynamics can be triggered and observed in real time at the window area. In particular, the morphology of electrodeposition layer and the growth front evolution are directly observed and correlated with the experimental parameters.[28-30] In the past years, substantial progress has been made to study the complex interactions between electron beam and the liquid samples,[31, 32] and to improve the imaging resolution in the liquid phase.[33, 34] Nevertheless, control of the chemical environment in the liquid cell (such as the concentration of the reactants and possible additives, the liquid flow rate and the pressure), remains a significant challenge. The difficulty is essentially associated with the bathtub like flow path design (Figure S1a, b). Fluid dynamics simulations show that the majority of the liquid bypasses the liquid cell (see the flower petal area in Figure S1a), while only a small portion of

the liquid diffuses into the cell.[35] Generally, such kind of liquid diffusion including the fluidic path and liquid volume in the cell is random, since it is highly dependent on many factors including the surface cleanliness of the chips, sample preparation on the chip, chip assembly steps, etc. Consequently, it is difficult to obtain reproducible results and achieve quantitative analysis. To address this issue, "on-chip flow" concept was proposed (Figure S1c, d).[25,26,30] The liquid is driven by an external pressure based pump and directed to flow between the chips and across the imaging window area, making it possible to obtain a well-controlled chemical environment in the liquid cell. In addition, the direct flow control enables to flush away unwanted electron beam induced species, to keep the electrolyte with a controlled concentration, and to flow other reactants into the liquid cell effectively.

In this work, we systematically demonstrated the control of chemical environment in a liquid TEM system. We studied the effect of different chemical environment in the liquid cell on the electrochemical deposition behavior of Cu crystals. The direct observations reveal that a higher liquid flow rate (1.38 μL min^{-1}) facilitates the deposition of a smooth layer on the electrode, while a lower liquid flow rate (0.1 μL min^{-1}) or the in-situ addition of $H_2PO_4^-$ ions promotes the dendritic Cu growth. The generality of this technique was further examined by studying Zn electrodeposition. The surface morphology evolution of Zn crystals in the liquid is controlled with the potential applied on the electrode and can be directly tracked and analysed at the nanoscale. Thanks to the well-controlled chemical environment, the present in-situ results provide new ideas to understand electrochemical nucleation, growth, phase formation and evolution, and give guidelines to design and synthesise nanostructures with specific morphology. Last but not least, the chemical environment control can be used as a new degree of freedom in liquid phase TEM, opening new venues for studying a wide range of dynamics.

2. Materials and Methods

2.1 Chemicals

To study the electrodeposition of Cu, an electrolyte of 20 mM $CuSO_4$ was prepared with the addition of 10 mM KH_2PO_4 aqueous solution. To study the electrolyte composition effect on the deposition morphology, pure $CuSO_4$ solution (20 mM) was also employed. Aqueous solution of $ZnSO_4$ with a concentration of 0.1 M was used as an electrolyte for the Zn deposition studies. Ultrapure water (Millipore Milli-Q grade) was used throughout the experiment.

2.2 Electrochemical TEM setup

Figure S2 displays a schematic illustration of the setup for electrochemical TEM studies (Stream LB, DENSsolutions, the Netherlands). A dual-chip liquid cell (termed Nano-Cell) composing a top chip and a bottom chip was used to seal the liquid. The windows on both chips are amorphous SiN_x with a thickness of 50 nm. For the top chip, the window orientation can be either parallel or orthogonal to the window on the bottom chip, resulting in a field of view with small (crossed windows) or larger (parallel windows) for different experimental purposes (Figure S3). On the bottom chip, there are spacers (200 nm in thickness), integrated liquid inlet, flow channel, and outlet. By connecting the holder with the assembled Nano-Cell to a gas pressure system via a polyetheretherketone (PEEK) tubing, the liquid sample can be driven from the inlet through the field of view and the outlet. This enables a good flow control, unlike the bathtub design in which the flow is governed by uncontrolled diffusion. The liquid flow rate can be controlled by independently changing the inlet and outlet pressure of the Nano-Cell.

For electrochemical studies, three platinum electrodes were patterned on the bottom chip, a working electrode (WE), reference electrode (RE) and counter electrode (CE). The electrodes were encapsulated with SiN_x except for the electrode area inside the microfluidic path, in order to prevent the possible interfacial side reactions occurred outside the window area. In addition, the holes present in each finger of the WE increase the electrode edge contact with the electrolyte, and create a confined reaction space,

making it possible to study the dynamics under different chemical environments.

For metallic electrodeposition, the counter electrode is usually made from the depositing material to replenish the electrolyte with the metallic cations. Therefore, we modified the current Pt CE electrochemically, by depositing a uniform layer of Cu or Zn (Figure S4) for the in-situ electrodeposition of Cu and Zn on WE. In principle, this electrode modification method is general, and the CE can be modified with any conductive material (metals, alloys, semiconductors, conductive polymers, etc).

2.3 In-situ TEM observations

The assembled holder with the Nano-Cell was leak-tested, and then inserted into a TEM (FEI Tecnai G^2 20, 120 kV, tungsten filament) for in-situ observations. Since the electron flux cannot be directly measured in our TEM, we can only qualitatively evaluate the effect of beam irradiation on the liquid sample and the electrochemical process, by setting the beam spot size at 1or 5. During each test, the beam intensity was kept constant. Chronoamperometric and cyclic voltammetry techniques were employed to perform the electrodeposition using a PalmSens 4 potentiostat. The dynamics were recorded by using an Olympus Megaview G2 camera, and captured by screen recording software (Camtasia). The post-processing and quantitative image analysis were performed using Fiji (ImageJ) software.

2.4 Post-mortem and ex-situ characterizations

After the in-situ experiments, the Nano-Cells were disassembled and the bottom chips were checked with a TEM (FEI Tecnai G^2 20, 120 kV, tungsten filament). Ex-situ studies were also performed by placing an electrolyte droplet on the bottom chip, and the electrochemical measurements were run with the same parameters used for the in-situ TEM. The product morphology on the bottom chip was examined by a scanning electron microscope (SEM, FEI Phenom, 10 kV).

3. Results and discussion

3.1 Demonstration of liquid flow capability

Chemical environment, such as the ion concentrations and the additives in a reaction space (conventional beaker, micro-/nano- fluidic channels, atomic scale interface, etc), affects the supersaturation of the solution and the electrochemical potential of chemical species, and thus plays an important role in the nucleation and growth during (electro)crystallization, as well as the device performance degradation. For conventional liquid phase TEM studies, control over the chemical environment is a challenge, as efficient liquid flow across the viewing area is lacking. This makes it difficult to investigate the effects of solution concentrations and additives on the liquid processes in real time. Thanks to the on-chip microfluidic design, the current liquid TEM system overcomes the limitation that the flow was dominated by uncontrolled diffusion. The TEM image sequence in Figure S5 (see also Movie S1) shows the process of liquid flowing inside the Nano-Cell with a constant flow rate ($\geq$ 8 μL min^{-1}). Before starting the flow, the Nano-Cell was assembled dry as demonstrated by the high contrast in the field of view (Figure S5a). The flow was initiated by turning on the pressure-based pump. During the flowing, the imaging parameters (magnification, focus, field of view, etc) were constant. After 20 s (Figure S5b) and 29 s (Figure S5c), there were no obvious changes in the TEM images, while after 30 s (Figure S5d), the imaging contrast changed abruptly, implying the liquid had flowed into the Nano-Cell. After that, the cell was filled with the liquid. Statistical analysis based on more than 20 experiments indicates that the time (t) to fill the Nano-Cell ranges from tens of seconds to 3 minutes when employing a flow rate of 8 μL min^{-1}. The efficient and well-controlled liquid flow establishes the prerequisite to observe liquid phenomena in TEM.

During imaging, the electron beam is employed to visualise the dynamics, meanwhile, it also influences the liquid and the objects suspended in liquid. Typical examples include bubble generation in the liquid cell,[36] and beam induced formation or etching of nanoparticles.[31] A generated bubble

reduces the local liquid thickness drastically, which can be beneficial for high-resolution imaging and analytical studies.[37] However, the bubble also creates additional liquid-gas interface, resulting in an inhomogeneous reaction environment. Our previous studies demonstrate that beam induced bubbles can be either flushed out by using the momentum of the liquid flow or dissolved into the liquid by controlling the gas pressures connected to the inlet and outlet.[25, 26] If metallic ions are present in the liquid, metal particles can be formed (mainly on the membranes) by capturing hydrated (solvated) electrons. These particles may interfere with the dynamics or reactions of interest, and also make it difficult to analyse the data afterwards.

On the other hand, with the controlled flow of our system, beam induced particles can be simply removed (Figure 1). To generate the particles, we increased the electron flux on purpose by changing the spot size from 5 (Figure S6) to 1 (Figure 1). When the flow was cut off (static state, 6.4 s – 11.4 s, Figure 1), the particles were formed and grew on the membrane, in agreement with previous electron beam-triggered nucleation and growth studies.[38] The observed phenomenon is induced by the supersaturation conditions and the diffusion-limited process. Firstly, when stopping the flow, the supersaturation of the solution increases, leading to a reduced critical radius. Therefore, the nucleation is easier than that with liquid flow case. In addition, the mass transportation is limited without the liquid flow. Under a high electron flux condition, the obtained crystals take a flower-like morphology rather than an equilibrium Wulff shape. Consecutively, the flow was switched on at 11.7 s and the particles stuck to the membrane were peeled off and moved from the top to the bottom area in the field of view (13.3 s and 13.8 s). It is interesting to find that the particles tend to be unstable in the liquid by decreasing the particle size until dissolving completely (19.5 s – 112.4 s). This may relate to the increased surface energy of the free particles and thus increased critical radius, causing the dissolution of the particles.[39]

In addition, the particles moving direction (13.3 s – 23.8 s) coincides with the flow direction (see

the yellow arrow), confirming the capability of the powerful liquid flow. It takes less than 2 min to "clean" the membrane by the continuous flushing, and this "writing via deposition"-"cleaning via flow" processes are reproducible as verified by performing additional flow ON and OFF cycles (Movie S2). The flow capability we presented here provides a useful tool to control the chemical environment in the liquid cell, and to study dynamics in the liquid environment.

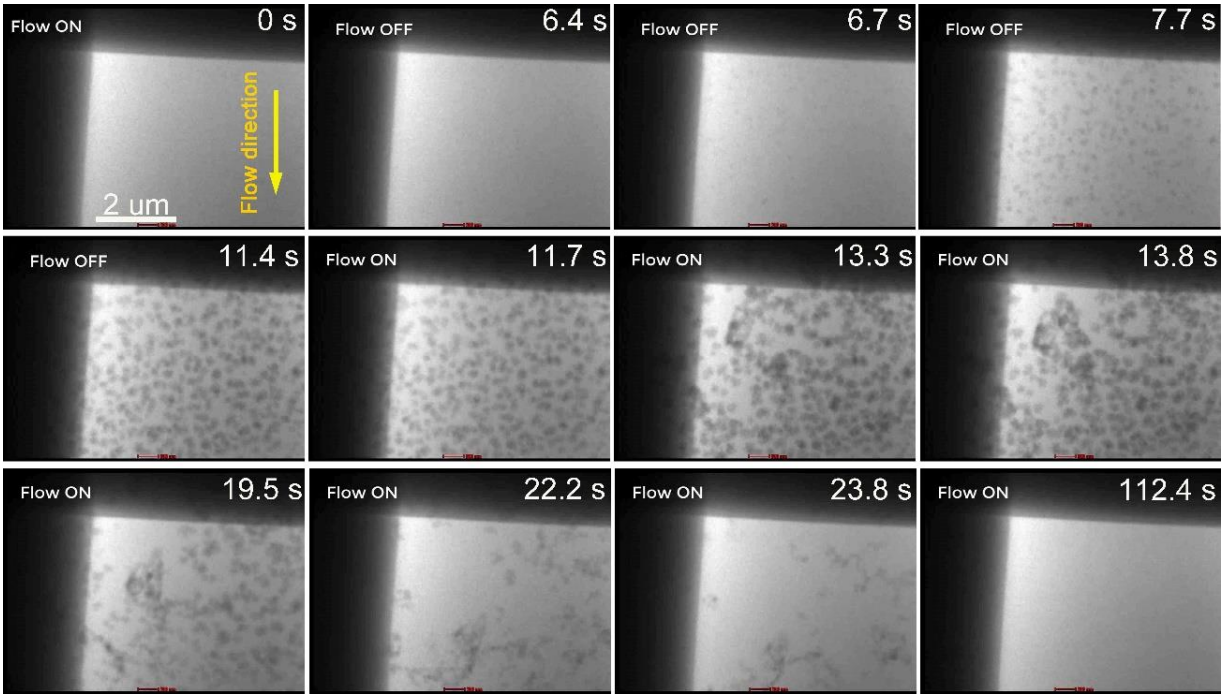

Figure 1. Time series of in situ TEM images showing the removing of electron beam induced nanoparticles by efficient liquid flow. The flow rate was 8 μL min^{-1} when the liquid was flowing ON. The liquid contains 20 mM $CuSO_4$ and 10 mM KH_2PO_4 aqueous solution.

3.2 Chemical environment affecting Cu electrodeposition

Since the liquid flow can be well controlled in the Nano-Cell, we can study the effect of flow rate on the electrochemical Cu crystallization and dissolution processes in real time. Figures. 2, 3 show time-lapse TEM images of the repeated Cu deposition and dissolution on the platinum WE at constant

potentials under specific flow rates. The WE was kept at +0.4 V (vs. Pt) in the initial 5 seconds to clean the electrode surface. After that, the deposition was triggered by applying a negative potential of -0.9 V (vs. Pt) for 10 s, which was followed by the dissolution at +0.4 V (vs. Pt) for 15 s. To study the repeatability, the deposition and dissolution cycle was run 4 times in the same field of view.

At a higher flow rate of 1.4 μL min^{-1} (see Figure 2, and Video S3), the Cu deposition and dissolution processes are reversible. Specifically, in the first 5 s, no obvious changes can be seen on the electrode edge and surface, due to the occurring of electro-oxidation reaction (or electrode cleaning). After this pre-treatment step, the Cu depositions were gradually formed on the WE edge at -0.9 V due to the reduction. The Cu layer coated on the Pt WE with a uniform thickness during the deposition process (5 – 15 s). Quantitative analysis indicates the layer growth rate is ~15.2 nm s^{-1}. By reversing the deposition potential to a positive value of +0.4 V, the Cu layer was dissolved into the electrolyte (15 – 30 s), and the dissolution took a conformal way, i.e., the Cu layer was oxidised layer-by-layer. In addition, it is found that the layer was dissolved completely after ~22 s, yielding a higher dissolution rate of ~21.4 nm s^{-1} than that of the growth rate. In the next 3 cycles, the deposition and dissolution showed similar behaviour as the first cycle (5 – 30 s), indicating the full reversibility of the electrochemical processes.

Besides the dynamics on the Pt WE, we also observed particle evolution away from the electrode. Before the experiment, there were three particles (I, II, and III as indicated by white arrows in Figure 2a) on the SiN_x membrane, which were formed by e-beam deposition. During the experiment, the particles keep growing. Since there was no direct contact between those particles with the electrode, size changing due to electrodeposition can be excluded. If considering the possible current leakage on the SiN_x membrane, the synchronised size increasing and decreasing of the particles with that of the layer changing on the Pt WE should be observed, but there is no obvious particle size decreasing. Therefore, the possible reason of those isolated particle changing is the heterogeneous nucleation and growth with

sufficient ions surrounding, which are provided by the higher liquid flow. This assumption is further confirmed by the control experiment that performed at a lower flow rate of 0.1 μL min^{-1} (see below).

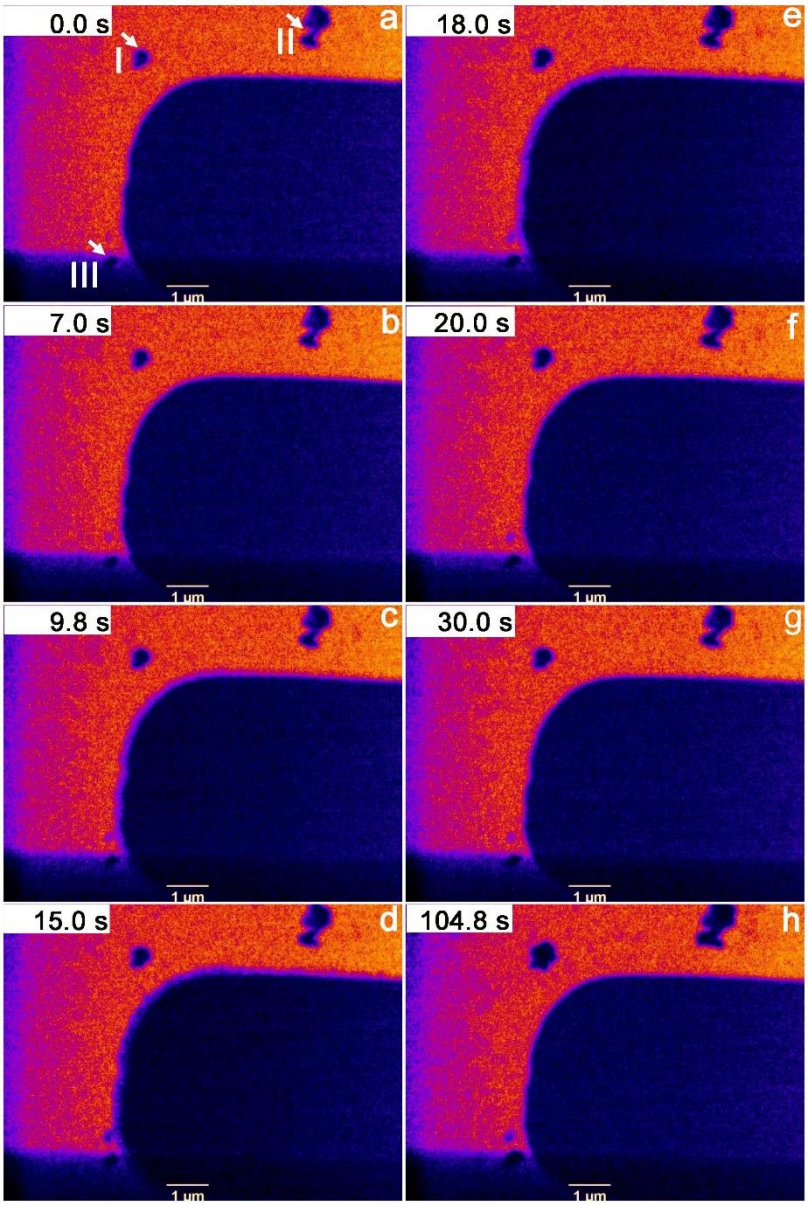

Figure 2. Time-lapse images showing the first cycle of growth (b-d, potential = -0.9 V, vs. Pt) and etching (e-g, potential = +0.4 V, vs. Pt) of Cu crystals on the Pt WE at a higher flow rate of 1.4 μL min^{-1}. (a) and (h) are images showing the morphology before and after the electrochemical operations. The full growth and etching processes (4 cycles) can be seen in Video S3. The electrolyte was 20 mM $CuSO_4$ aqueous solution with the addition of 10 mM KH_2PO_4. The temperature colours are used to improve the

contrast.

We decreased the flow rate to 0.1 μL min^{-1} (see Figure 3, and Video S4) to study the deposition and dissolution processes for Cu on the same field of view. The protocol, including the initial electrode cleaning, deposition (-0.9 V, 10 s), dissolution (+0.4 V, 15 s), and repeating for 4 cycles, is identical with the case of the higher flow rate of 1.4 μL min^{-1}. Several differences can be distinguished in this limited liquid supply condition. (1) In the first growth step (5 – 15 s), the Cu deposition was not smooth or uniform along the WE. Especially close to the electrode tip area, the deposition showed dendrite-like morphology. (2) The dissolution (15 – 30 s) starts from deposition-WE interface rather than the front of deposition in electrolyte, and the dissolution is not complete. Obviously, there are several particles left after the first dissolution (indicated by black arrows in Figure 3g). Those residual particles ("dead copper") that lose contact with the Pt WE are in close analogy to "dead lithium" as studied in lithium-ion (or lithium metal) batteries [40]. (3) In the following depositions, those "dead copper" particles act as new nucleation sites. When the depositions reach the "dead" particles, the growth speed is increased. (4) After 4 cycles, the "dead copper" size increased significantly due to the continuous agglomeration of the new "dead" depositions (106.8 s, Figure 3h). The growth of dead depositions is one of the important reasons for the capacity loss under long term battery operation. Meanwhile, the accelerated dead depositions growth rate should also be responsible for the battery safety issue.

There are several mechanisms governing dendrite growth of electrodeposited metals,[41, 42] such as the limited ion/mass diffusion and the blocked electron transfer. During electrodeposition, a diffusion dominated situation can be achieved at a high overpotential or by increasing the diffusion layer thickness. In our studies, the effective diffusion thickness is increased under the limited flow rate, which results in dendrite formation [43]. The diffusion-controlled transportation also leads to a non-uniform ion

concentration distribution surrounding the dendrites.[44] Therefore, the oxidation potential along the deposition varies according to the studies by Sasaki et al,[45] and the non-uniform dissolution and the formation of "dead copper" happen consequently. We also noticed that the isolated three particles (I, II, and III as indicated by white arrows in Figure 3a) did not experience any morphology change, which is completely different than the observations shown at a higher liquid flow rate of 1.4 μL min^{-1} (Figure 2). The results demonstrate the limited ion/mass transportation under the lower flow rate condition.

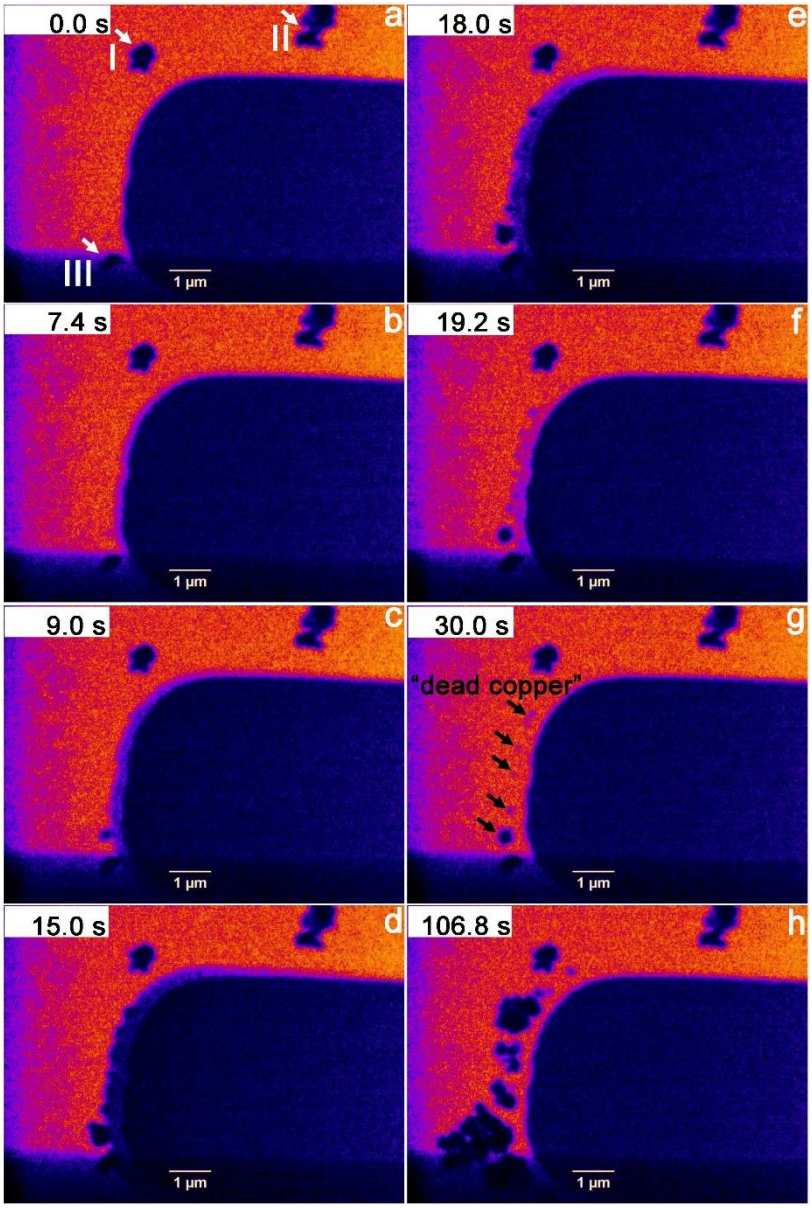

Figure 3. Time-lapse images showing the first cycle of growth (b-d, potential = -0.9 V, vs. Pt) and

etching (e-g, potential = +0.4 V, vs. Pt) of Cu crystals on the Pt WE at a lower flow rate of 0.1 μL min^{-1}. (a) and (h) are images showing the morphology before and after the electrochemical operations. The full growth and etching processes (4 cycles) can be seen in Video S4. The electrolyte was 20 mM $CuSO_4$ aqueous solution with the addition of 10 mM KH_2PO_4. The temperature colours are used to improve the contrast.

Besides flow rate and electrolyte composition, a third major influential factor in electrochemical deposition is the presence of foreign additives. Such additives, like inorganic ions or organic ligands, affect the electrochemically deposited crystals by changing the nuclei structures (single crystals, twins, or stacking faults), and/or selective adsorption on specific planes.[3, 18-20] By employing liquid cell TEM, Arán-Ais and coworkers [21] directly observed that the addition of Cl^- ions in 5mM $CuSO_4$ electrolyte led to the formation of co-existed Cu_2O cubes and other irregular morphologies during the cathode scanning. In the following oxidation process, the Cu_2O particles with irregular morphologies dissolved due to the high surface activity, leaving Cu_2O cubes on the WE.

In our previous in-situ TEM study, [10] we also demonstrated that the presence of $H_2PO_4^-$ ions in 20 mM $CuSO_4$ aqueous solution significantly alters the morphology of the deposited Cu crystals. The results indicate a smoother growth at a lower potential of -0.64 V, vs. Au in the absence of $H_2PO_4^-$ ions. At a higher potential of -0.74 V, vs. Au, the deposition shows a coarse surface, which is constituted by big Cu granules. By adding 10 mM KH_2PO_4, we obtained Cu dendrites even at a low potential of -0.64 V, vs. Au, highlighting the importance of $H_2PO_4^-$ ions as a morphology directing agent.

In these works, to study the electrodeposition under different electrolytes, multiple liquid cells were employed, which makes it challenging to keep the liquid cell environment unchanged, especially regarding liquid thickness. This limitation can be overcome due to the efficient liquid flow control of

our system. We firstly studied the electrodeposition of Cu from pure $CuSO_4$ aqueous solution. After the Nano-Cell was filled with the electrolyte, the flow was stopped to keep the cell in a static state. As shown in Movie S5, the Cu crystals were grown on the Pt WE under a potential of -0.6 V, vs. Pt. No obvious dendritic morphology, but only granules were formed (average size ~100 nm, Figure 4 Left). After the experiment, the electrolyte in the sample source was replaced by the mixture of $CuSO_4$ and KH_2PO_4 solution. The liquid was kept flowing with a flow rate of 3 $\mu L min^{-1}$ for 15 min. In this way, we could directly study the electrolyte effect on the depositions in the same liquid cell by excluding all the uncertainties during different cells assembly. Movie S6 shows the growth process of Cu dendrites on the Pt WE at an applied potential of -0.6 V, vs. Pt. In the beginning, Cu granules randomly deposited and grew continuously. Then dendritic crystals formed on some of the granules' surface and extended into the electrolyte (Figure 4 Right). The addition of $H_2PO_4^-$ ions in the electrolyte leads to the formation of Cu-phosphate complexes. Such process competes with the electrochemical deposition for the free Cu^{2+} ions in the solution and leading to the formation of Cu dendrites. It should be mentioned here that although the reference electrode used here (Pt) is different from the previous work (Au) [10], the observed results are consistent, i.e., Cu dendrites can be deposited at a lower potential with the addition of $H_2PO_4^-$ ions. It further confirms the importance of electrolyte composition modulation, and demonstrates the effectiveness of the environment control of the liquid TEM system.

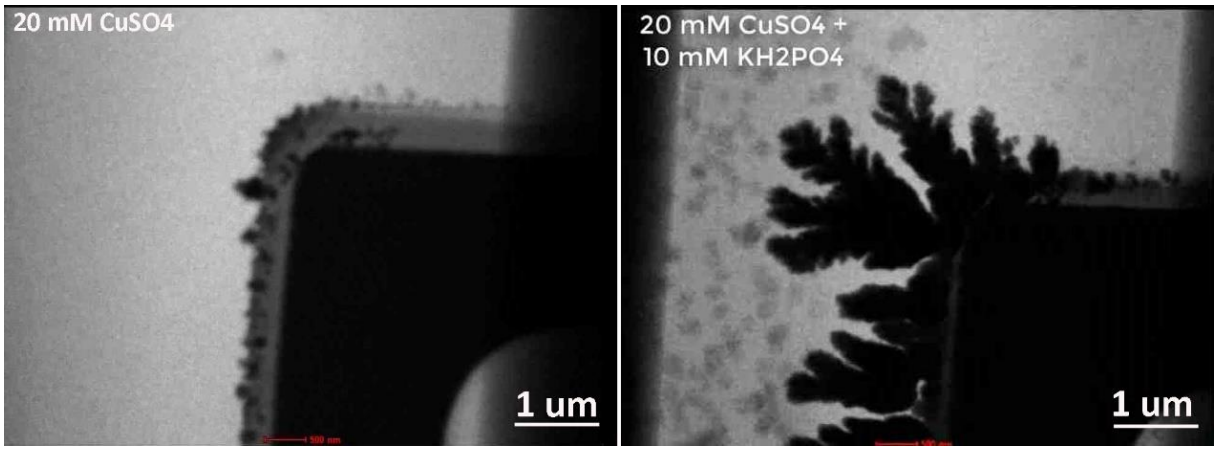

Figure 4. The effect of phosphate addition on Cu deposition. (Left) TEM image of Cu granules on the Pt WE deposited from an aqueous solution of 20 mM $CuSO_4$ with an applied potential of -0.6 V, vs. Pt. (Right) TEM image of the Cu dendrites deposited using the mixed solution of 20 mM $CuSO_4$ and 10 mM KH_2PO_4 with the same applied potential of -0.6 V, vs. Pt.

3.3 Potential controlled Zn electrodeposition

To further explore the applications of the system, we studied the electrochemical deposition of zinc from an aqueous solution of 0.1 M $ZnSO_4$. The experiment was performed without liquid flow, i.e., in a static state. Figure S7 shows a representative cyclic voltammetry curve for the deposition and etching of Zn. The potential was scanned from +0.25 V (vs. Pt) in the negative direction with a potential range of -1.5 V and +0.8 V, vs. Pt. Movie S7 and the TEM image series displayed in Figure 5 show the corresponding evolution of the deposition.

At 0.0 s, the electrode surface is clean, and no depositions are formed, since the electrode is in an oxidate state (+0.25 V). When the potential is ramped to -0.25 V, bright spots appear on the edge of the electrode, the initial nucleation sites (see the white arrows at 5.0 s). This change correlates to the minor cathode peak at ~-0.25 V in the CV curve. At a potential of -0.31 V (5.6 s), a layer starts coating the

edges of the electrode (including the outer edge and the inner circle edge). In addition, the contrast change on the electrode surface indicates that the electrocrystalline event also happens on the projected surface. From -0.51 V (7.6 s) to -0.73 V (8.8 s), both the depositions on the electrode edge and surface grow steadily. When the potential is increased to -0.89 V (10.4 s), noticeable dendrites are obtained and extended into the electrolyte when further scanning the potential to -0.95 V (11.0 s). This rapid growth is in good agreement with the appearance of a major reduction peak at ~-1.0 V shown in the CV curve (Figure S7).

It is interesting to find that the dendrite formation sites are not uniform on the initial deposition layer, but only on some specific positions. To clarify the preferred location for the dendrite's growth, we schematically draw lines on the deposition layer before the dendrites formed (7.6 s), where the length and direction of the lines correspond to the dendrites' trunk dimension and growth orientation (11.0 s). It is clear to see that most of the dendrite growth starts from convex spots. Compared to flat or concave areas on the electrode, the convex spots have higher concentration of mass and charge, which are responsible for the rapid growth of crystals with kinetic anisotropic morphology [11]. There are also some convex positions (see the yellow arrows at 7.6 s) that are not active for the following dendrites growth. This could relate to the steric hindrance of the neighboring dendrites and the ion depletion in the reaction front. Our in-situ studies indicate that regulating the surface roughness of the substrates is useful to modulate homogeneous nucleation and to obtain uniform electrodeposits with smooth dendrite-free morphology. Experimentally, coating the substrates with protective materials [46], texturing the substrate surface [47], or modifying the electrolyte [48] have been successfully employed to reach a planar substrate-electrolyte interface and thus a homogeneous Zn deposition.

In the following anodic scan, the oxidation reaction occurs on the WE. The oxidation current is not noticeable at -1.39 V (18.6 s) and no obvious morphology changes can be observed. Further increasing

the potential to -1.37 V, the depositions are rapidly stripped. At -1.35 V (19.0 s), close to the first oxidation peak (-1.34 V, Figure S7), the deposition layer connected to the edge of the Pt WE is stripped completely. The decreased contrast of the Pt WE also suggests the dissolution of the Zn depositions on the electrode surface, but there is still some residual Zn left on the surface, indicating that the surface depositions are more stable than those on the edge of the electrode. Those residual Zn layers can be completely stripped at a higher anodic potential (+0.29 V, 35.4 s, and +0.39 V, 36.4 s). Again, we observed the dead zinc during the stripping process (-1.35 V, 19.0 s), similar to that of electrochemical deposition/etching of Cu as we have shown above. However, when compared to the dead Cu, the dead Zn depositions are not stable as they are dissolved during imaging. This probably relates to the amphoteric nature of the zinc metal that reacts with the e-beam irradiated liquid (pH < 7) and ultimately dissolves.

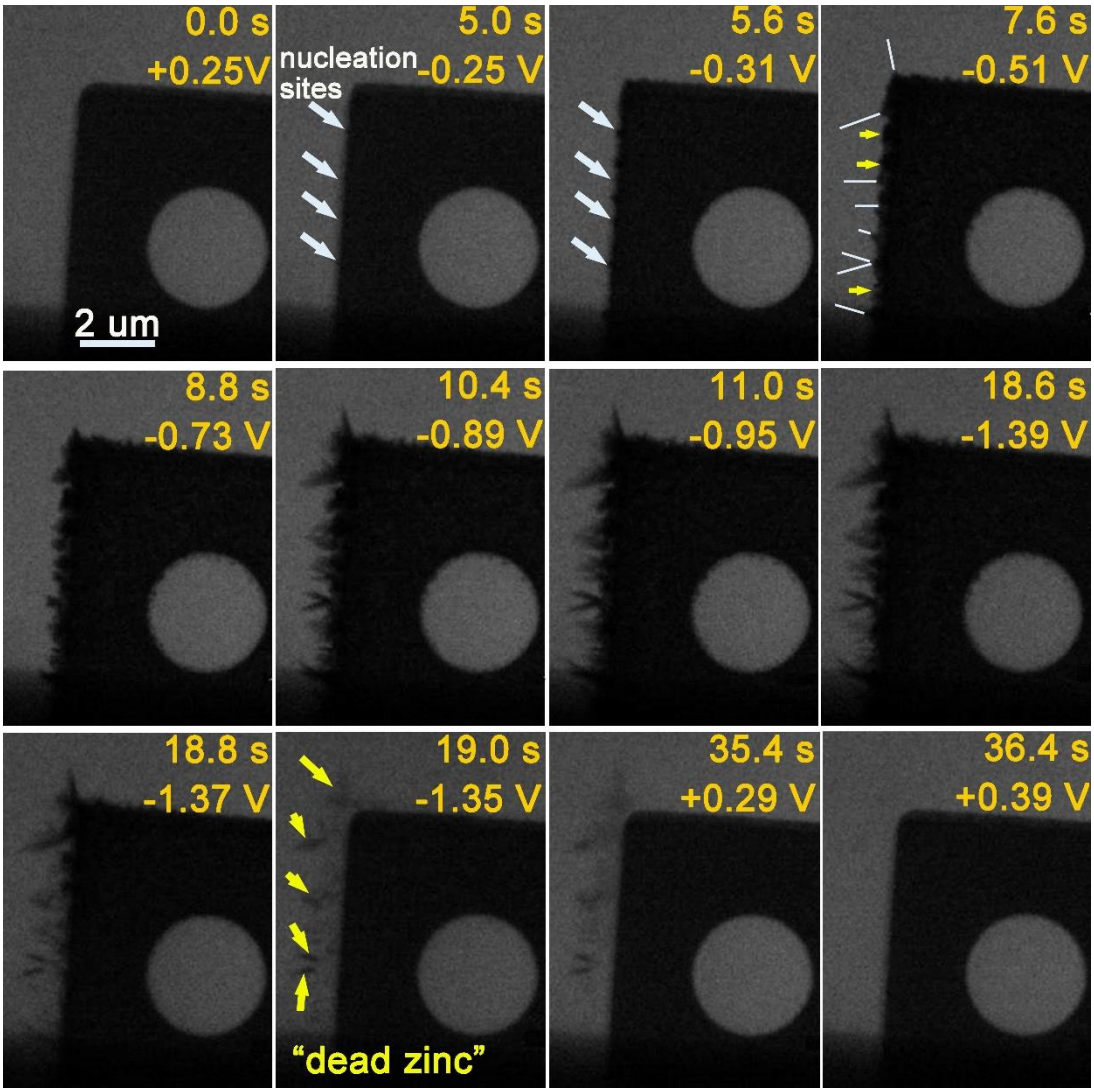

Figure 5. TEM image series showing Zn deposition and etching on the Pt WE. The potential window of -1.5 V to +0.8 V, vs. Pt was scanned at 100 mV s^{-1}. The electrolyte was 0.1 M $ZnSO_4$ aqueous solution and was kept at a static state during the experiment.

Based on the above voltammetric results, we investigated the potential controlled deposition of Zn in real time. We set the potential at -0.9 V for 10 s to start the deposition , followed by another 10 s at a higher potential of -1.1 V for. Figure 6a displays the main results for the successive deposition processes (see also Movie S8) by applying the low (upper panel) and high (low panel) potentials. At -0.9 V, steady growth is observed from the edges of the inner and outer electrode surface (see the blue color). Comparing to the outer edge, the deposition on the inner edge is rougher (Figure 6b), which could be

due to the limited ion supply in the confined reaction space, resulting in a kinetically controlled crystalline growth. In the following growth at -1.1 V, dendritic depositions are nucleated and grown on the previous outer edge, while no further growth can be observed in the inner edge (Figure 6c). This means that the ions are consumed during the growth at the lower potential of -0.9 V, and no new ions can be replenished due to the space confinement in the inner circle. Therefore, by using the current electrode design, we can explore rich liquid dynamics within different chemical environments.

The potential controlled growth of Zn depositions can be well described by the classical electrocrystallization theory.[49, 50] When the applied potential is lower (-0.9 V), the slow diffusing process and growth rate of the crystals facilitate the steady migration of the atoms. This favors the depositions with a smooth surface. With a potential of -1.1 V, the rapid growth of the Zn layer results in a kinetically controlled morphology (dendrites). Similar potential or current density-controlled electrodeposition has also been confirmed by different ex-situ studies.[20]

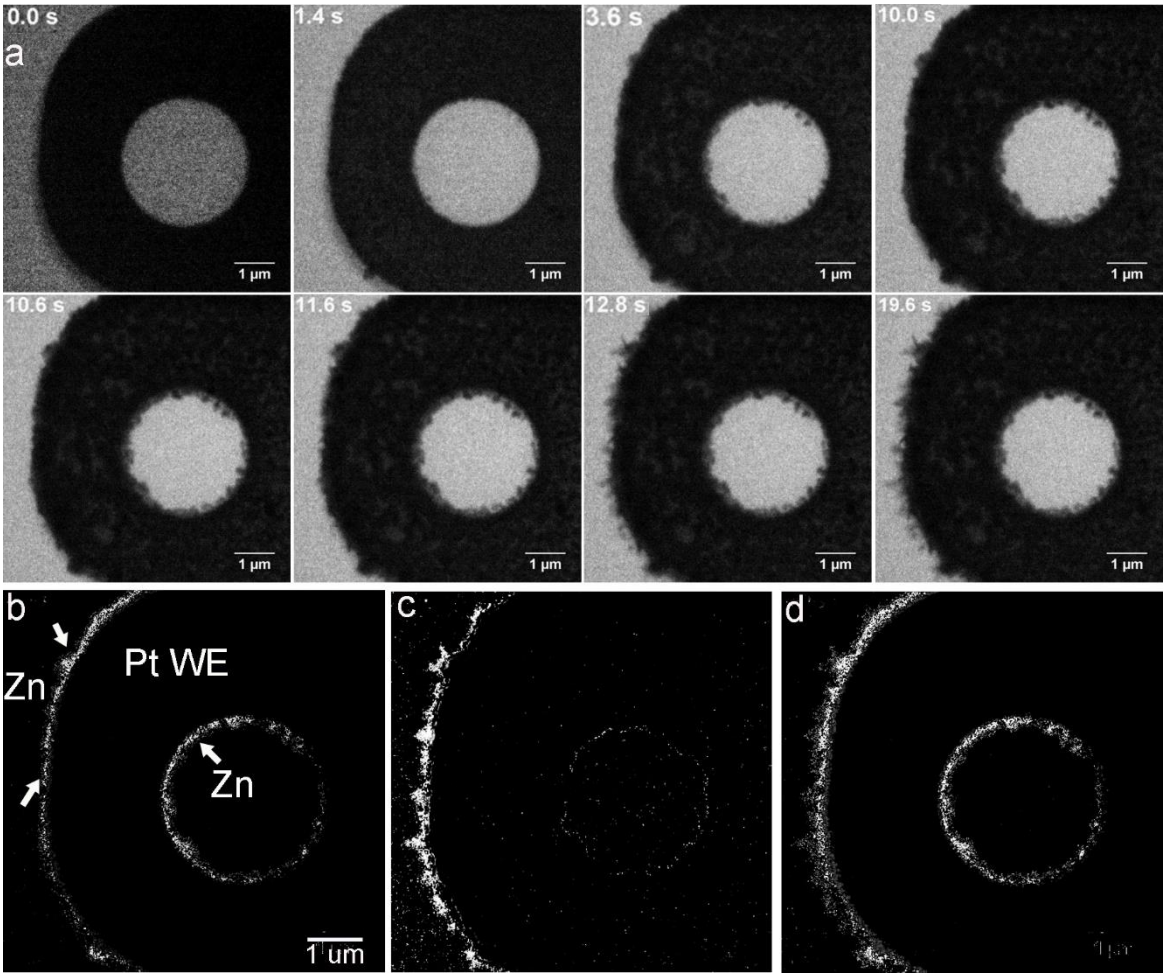

Figure 6. (a) Successive growth of Zn layers on the Pt WE at a lower potential of -0.9 V, vs. Pt (0 – 10 s) and the following growth at a higher potential of -1.1 V, vs. Pt (10 - 20 s). The electrolyte was 0.1 M $ZnSO_4$ aqueous solution and was kept at a static state during the experiment. The total growth of Zn layer at (b) a lower potential of -0.9 V (vs. Pt) in the first 10 s, and (c) a higher potential of -1.1 V (vs. Pt) in the second 10 s. (d) showing the total growth of Zn depositions in the 20 s. Figures (b)-(d) were generated by image analysis performed on image sequences taken from Movie S8. Individual frames are saved as 8-bit grayscale (0–255) matrix and then smoothed. Figures (b), (c), and (d) are yielded by subtracting 0.0 s frame from 10.0 s frame, 10.0 s frame from 20.0 s frame, and 0.0 s frame from 20.0 s frame, respectively. A binary threshold is used to improve the contrast.

The Zn depositions were analysed post-mortem by disassembling the Nano-Cell and cleaning and drying the chips. Figure S8a-e illustrates representative TEM images of the results. The bright field and dark field images show that the Zn crystals are formed on the electrode edge as well as on the surface (see the white arrows in Figure S8c), which agrees well with the in-situ observations. Moreover, there are Zn plates present on the membrane away from the electrode, which may have detached during the cleaning process. The measured corner angle is ~120º, indicating 2D growth along the base plane of the Zn crystals (Figure S8f). The result is also supported by the electron diffraction (Figure S8e inset). The result hints that the Zn depositions may consist of 2D nanosheets. For comparison, we performed ex-situ experiments by putting a droplet of the electrolyte (5 μL in volume) on the bottom chip, and applying a potential of -1.1 V for 20 s. SEM characterization (Figure S9) shows that the depositions possess dendritic morphology, and each branch is assembled by regular hexagonal nanosheets. Although the ex-situ results are consistent with the in-situ observations, the effects of other experimental conditions on the depositions, especially liquid thickness, should be carefully evaluated via more experimental and theoretical studies.

4. Conclusions

In summary, by designing a new liquid TEM system, we successfully achieved control of the chemical environment inside our liquid cell for in-situ TEM studies. The effects of liquid flow, flow rate, electrolyte composition, and electrochemical potential on the deposition and dissolution processes of Cu crystals were studied in detail. To demonstrate the generality, we furthermore studied the electrodeposition of Zn crystals. We have shown for both Cu and Zn that the growth behavior can be controlled. Our studies enrich the existing liquid phase TEM and ex-situ results, and provide new insights in materials synthesis and device applications. We also mention that the methodology developed

in our low-end microscope can be directly used in high-end microscopes, making it possible to study chemical composition and electronic structure at high resolution.

Data availability statement

The data that support the findings of this study are available upon reasonable request from the authors.

Appendix A. Supplementary data

Supplementary data to this article can be found online.

References

[1] D. Huo, M. J. Kim, Z. Lyu, Y. Shi, B. J. Wiley, Y. Xia, Chem. Rev. 119 (2019) 8972–9073.

[2] Z. Fan, X. Huang, C. Tan, H. Zhang, Chem. Sci. 6 (2015) 95–111.

[3] Y. Xia, Y. Xiong, B. Lim, S. E. Skrabalak, Angew. Chem. Int. Ed. 48 (2009) 60–103.

[4] A. R. Tao, S. Habas, P. Yang, Small 4 (2008) 310–325.

[5] A. Dutta, M. Rahaman, N. C. Luedi, M. Mohos, P. Broekmann, ACS Catalysis 6 (2016) 3804–3814.

[6] N.-T. Suen, Z.-R. Kong, C.-S. Hsu, H.-C. Chen, C.-W. Tung, Y.-R. Lu, C.-L. Dong, C.-C. Shen, J.-C. Chung, H. M. Chen, ACS Catalysis 9 (2019) 5217–5222.

[7] J. Choi, M. J. Kim, S. H. Ahn, I. Choi, J. H. Jang, Y. S. Ham, J. J. Kim, S.-K. Kim, Chem. Eng. J. 299 (2016) 37–44.

[8] B. C. Marepally, C. Ampelli, C. Genovese, F. Tavella, E. A. Quadrelli, S. Perathoner, G. Centi, J. CO_2 Util. 35 (2020) 194–204.

[9] T. N. Huan, P. Simon, G. Rousse, I. Génois, V. Artero, M. Fontecave, Chem. Sci. 8 (2017) 742–747.

[10] J. Zhao, L. Sun, S. Canepa, H. Sun, M. N. Yesibolati, M. Sherburne, R. Xu, T. Sritharan, J. S. C. Loo, J. W. Ager Iii, J. Barber, K. Mølhave, Z. J. Xu, J. Mater. Chem. A 5 (2017) 11905–11916.

[11] M. Liu, Y. Pang, B. Zhang, P. De Luna, O. Voznyy, J. Xu, X. Zheng, C. T. Dinh, F. Fan, C. Cao, F. P. G. de Arquer, T. S. Safaei, A. Mepham, A. Klinkova, E. Kumacheva, T. Filleter, D. Sinton, S. O. Kelley, E. H. Sargent,

Nature 537 (2016) 382–386.

[12] P. Hundekar, R. Jain, A. S. Lakhnot, N. Koratkar, J. Appl. Phys. 128 (2020) 010903/1–12.

[13] Q. Yang, Q. Li, Z. Liu, D. Wang, Y. Guo, X. Li, Y. Tang, H. Li, B. Dong, C. Zhi, Adv. Mater. 32 (2020) 2001854/1–32.

[14] L. Péter, Electrochemical Methods of Nanostructure Preparation, Springer International Publishing, 2021.

[15] M. J. Kim, M. Brown, B. J. Wiley, Nanoscale 11 (2019) 21709–21723.

[16] H. Sun, X. Li, Y. Chen, W. Li, F. Li, B. Liu, X. Zhang, Nanotechnology 19 (2008) 225601/1–8.

[17] H. Sun, Y. Yu, M. Ahmad, Mater. Lett. 65 (2011) 3482–3485.

[18] M. Haataja, D. J. Srolovitz, Phys. Rev. Lett. 89 (2002) 215509/1–4.

[19] M. Haataja, D. J. Srolovitz, A. B. Bocarsly, J. Electrochem. Soc. 150 (2003) C708–C716.

[20] M. T. Strand, T. S. Hernandez, M. G. Danner, A. L. Yeang, N. Jarvey, C. J. Barile, M. D. McGehee, Nat. Energy 6 (2021) 546–554.

[21] R. M. Arán-Ais, R. Rizo, P. Grosse, G. Algara-Siller, K. Dembélé, M. Plodinec, T. Lunkenbein, S. W. Chee, B. R. Cuenya, Nat. Commun. 11 (2020) 3489/1–8.

[22] M. Ross Frances, Science 350 (2015), aaa9886.

[23] M. J. Williamson, R. M. Tromp, P. M. Vereecken, R. Hull, F. M. Ross, Nat. Mater. 2 (2003) 532–536.

[24] M. Y. Jong, J. Park, P. Ercius, K. Kim, J. H. Daniel, F. C. Michael, Y. L. Jeong, A. Zettl, A. P. Alivisatos, Science 336 (2012) 61–64.

[25] A. F. Beker, H. Sun, M. Lemang, J. T. van Omme, R. G. Spruit, M. Bremmer, S. Basak, H. H. Pérez Garza, Nanoscale 12 (2020) 22192–22201.

[26] J. T. van Omme, H. Wu, H. Sun, A. F. Beker, M. Lemang, R. G. Spruit, S. P. Maddala, A. Rakowski, H. Friedrich, J. P. Patterson, H. H. Pérez Garza, J. Mater. Chem. C 8 (2020) 10781–10790.

[27] S. Canepa, M. N. Yesibolati, J. Schiøtz, S. Kadkhodazadeh, W. Huang, H. Sun, K. Mølhave, ACS Appl. Nano Mater. 4 (2021) 12346–12355.

[28] B. L. Mehdi, J. Qian, E. Nasybulin, C. Park, D. A. Welch, R. Faller, H. Mehta, W. A. Henderson, W. Xu, C. M. Wang, J. E. Evans, J. Liu, J. -G. Zhang, K. T. Mueller, N. D. Browning, Nano Lett. 15 (2015) 2168–2173.

[29] J. H. Park, N. M. Schneider, D. A. Steingart, H. Deligianni, S. Kodambaka, F. M. Ross, Nano Lett. 18 (2018) 1093–1098.

[30] M. Li, L. Ran, R. Knibbe, J. Phys. Chem. Lett. 12 (2021) 913–918.

[31] N. M. Schneider, M. M. Norton, B. J. Mendel, J. M. Grogan, F. M. Ross, H. H. Bau, J. Phys. Chem. C 118 (2014) 22373–22382.

[32] J. Lee, D. Nicholls, N. D. Browning, B. L. Mehdi, Phys. Chem. Chem. Phys. 23 (2021) 17766–17773.

[33] S. Keskin, P. Kunnas, N. de Jonge, Nano Lett. 19 (2019) 4608–4613.

[34] H. Wu, H. Su, R. R. M. Joosten, A. D. A. Keizer, L. S. van Hazendonk, M. J. M. Wirix, J. P. Patterson, J. Laven, G. de With, H. Friedrich, Small Methods 5 (2021) 2001287/1–9.

[35] G. Marchello, C. Pace, N. Wilkinson, L. Ruiz-Perez, G. Battaglia, (Preprint) arXiv:1907.03348, submitted: July 2019.

[36] J. M. Grogan, N. M. Schneider, F. M. Ross, H. H. Bau, Nano Lett. 14 (2014) 359–364.

[37] G. Zhu, Y. Jiang, W. Huang, H. Zhang, F. Lin, C. Jin, Chem. Commun. 49 (2013) 10944–10946.

[38] H. Zheng, R. K. Smith, Y.-W. Jun, C. Kisielowski, U. Dahmen, A. P. Alivisatos, Science 324 (2009) 1309–1312.

[39] N. T. K. Thanh, N. Maclean, S. Mahiddine, Chem. Rev. 114 (2014) 7610–7630.

[40] C. Fang, J. Li, M. Zhang, Y. Zhang, F. Yang, J. Z. Lee, M.-H. Lee, J. Alvarado, M. A. Schroeder, Y. Yang, B. Lu, N. Williams, M. Ceja, L. Yang, M. Cai, J. Gu, K. Xu, X. Wang, Y. S. Meng, Nature 572 (2019) 511–515.

[41] K. Wang, ACS Omega 5 (2020) 10225–10227.

[42] K. Popov, P. Živković, N. Nikolić, Zastita Materijala 57 (2016) 55–62.

[43] J. Ji, P. Li, S. Sang, W. Zhang, Z. Zhou, X. Yang, H. Dong, G. Li, J. Hu, AIP Adv. 4 (2014) 031329/1–9.

[44] C. Lupo, D. Schlettwein, J. Electrochem. Soc. 166 (2018) D3182–D3189.

[45] Y. Sasaki, K. Yoshida, T. Kawasaki, A. Kuwabara, Y. Ukyo, Y. Ikuhara, J. Power Sources 481 (2021) 228831/1–7.

[46] J. Zheng, D. C. Bock, T. Tang, Q. Zhao, J. Yin, K. R. Tallman, G. Wheeler, X. Liu, Y. Deng, S. Jin, A. C. Marschilok, E. S. Takeuchi, K. J. Takeuchi, L. A. Archer, Nat. Energy 6 (2021) 398–406.

[47] S. Li, J. Fu, G. Miao, S. Wang, W. Zhao, Z. Wu, Y. Zhang, X. Yang, Adv. Mater. 33 (2021) 2008424/1–9.

[48] X. Guo, Z. Zhang, J. Li, N. Luo, G. -L. Chai, T. S. Miller, F. Lai, P. Shearing, D. J. L. Brett, D. Han, Z. Weng, G. He, I. P. Parkin, ACS Energy Lett. 6 (2021) 395–403.

[49] W. J. Lorenz, G. Staikov, Surf. Sci. 335 (1995) 32–43.

[50] A. Milchev, Electrocrystallization: Fundamentals of Nucleation and Growth, Springer US, 2002.